Nuclear energy density optimization: Large deformations

M. Kortelainen,[1,2] J. McDonnell,[1,2] W. Nazarewicz,[1,2,3] P.-G. Reinhard,[4] J. Sarich,[5] N. Schunck,[1,2,6]
M. V. Stoitsov,[1,2] and S. M. Wild[5]

[1]*Department of Physics and Astronomy, University of Tennessee, Knoxville, Tennessee 37996, USA*
[2]*Physics Division, Oak Ridge National Laboratory, P.O. Box 2008, Oak Ridge, Tennessee 37831, USA*
[3]*Institute of Theoretical Physics, Warsaw University, ul. Hoża 69, PL-00681, Warsaw, Poland*
[4]*Institut für Theoretische Physik, Universität Erlangen, D-91054 Erlangen, Germany*
[5]*Mathematics and Computer Science Division, Argonne National Laboratory, Argonne, Illinois 60439, USA*
[6]*Physics Division, Lawrence Livermore National Laboratory, Livermore, California 94551, USA*

(Received 18 November 2011; published 8 February 2012)

A new Skyrme-like energy density suitable for studies of strongly elongated nuclei was determined in the framework of the Hartree-Fock-Bogoliubov theory using the recently developed model-based, derivative-free optimization algorithm POUNDerS. A sensitivity analysis at the optimal solution has revealed the importance of states at large deformations in driving the parameterization of the functional. The good agreement with experimental data on masses and separation energies, achieved with the previous parameterization UNEDF0, is largely preserved. In addition, the new energy density UNEDF1 gives a much improved description of the fission barriers in ^{240}Pu and neighboring nuclei.

DOI: 10.1103/PhysRevC.85.024304 PACS number(s): 21.60.Jz, 21.30.Fe, 21.65.Mn, 24.75.+i

I. INTRODUCTION

One of the focus areas of the UNEDF SciDAC collaboration [1,2] was the description of the fission process within a self-consistent framework based on nuclear density functional theory (DFT). Until now, attempts at going beyond the macroscopic-microscopic methods [3] have been carried in the context of the original self-consistent nuclear mean-field theory [4] with Skyrme (see, e.g., Refs. [5–10]), Gogny (see, e.g., Refs. [11–14]), and relativistic (see, e.g., Refs. [5,15,16]) energy density functionals (EDFs). The fundamental assumption of the nuclear DFT is that one can describe accurately a broad range of phenomena in nuclei, including excited states and large-amplitude collective motion, by enriching the density dependence of the functional while staying at the single-reference Hartree-Fock-Bogoliubov (HFB) level. In this picture, beyond-mean-field corrections are implicitly built in. Preliminary studies aimed at re-examining the old problem of restoring broken symmetries in this context are promising [17,18].

A common challenge to both the self-consistent mean field and the DFT approach is the need to carefully optimize the EDF parameters to the preselected pool of observables [4,19–25]. In particular, special attention must be paid to optimize the parameters in the same regime where the theory will later be applied and to choose the fit observables accordingly. In a recent work [26], we showed that existing Skyrme EDFs exhibit a significant spread in bulk deformation properties, and re-emphasized [27,28] that the resulting theoretical uncertainties could be greatly reduced by considering data corresponding to large deformation in the optimization process. Let us recall that the early Skyrme-type EDF SkM* [29] was in fact optimized for fission studies in the actinide region by considering the experimental information on the fission barrier of ^{240}Pu. However, the optimization was not performed directly at the deformed HFB level; instead, a semiclassical approach was used based on the Thomas-Fermi approximation together with shell-correction techniques. The D1S parameterization of the finite-range Gogny force was also fine-tuned to the first barrier height of ^{240}Pu [30], considering a rotational correction to the energy of the deformed state. However, this fine-tuning again was not done directly at the HFB level but by a manual readjustment of the surface coefficient of the EDF using a phenomenological model. Also, in the Bsk14 EDF of the HFB-14 mass model [31] by the Bruxelles-Montréal collaboration, data on fission barriers were utilized to optimize the EDF parameters by adding phenomenological collective corrections, including a rotational one. One may, therefore, conclude that no EDF has ever been systematically optimized at the deformed HFB level (and without phenomenological corrections added) by explicitly considering constraints on states at large deformations.

In a previous study [25], we applied modern optimization and statistical methods, together with high-performance computing, to carry out EDF optimization at the deformed HFB level, namely, the approximation level where the functional is later applied. The resulting EDF parameterization UNEDF0 yields good agreement with experimental masses, radii, and deformations. The present work represents an extension of Ref. [25] to the problem of fission. In particular, it builds on the results reported in Ref. [26], which concluded that the data on strongly deformed nuclear states should be considered in the optimization protocol to constrain the surface properties of the functional.

Here we propose the new EDF Skyrme parameterization, UNEDF1, which is obtained by adding to the list of fit observables the experimental excitation energies of fission isomers in the actinides. To ensure that the functional can be used in fission and fusion studies, we have removed the center-of-mass (c.m.) correction in the spirit of the DFT. As in the case of UNEDF0, a sensitivity analysis has been performed at the solution to identify possible correlations between model

parameters and assess the impact of the new class of fit observables on the resulting parameterization.

This paper is organized as follows. In Sec. II we briefly review the theoretical framework, establish the notation, and justify the removal of the c.m. correction. Section III defines the set of fit observables, discusses numerical precision and implementation, and presents the new UNEDF1 parameter set together with the results of the sensitivity analysis. To assess the impact of fission-isomer data, we compare UNEDF1 with UNEDF0 in Sec. IV. In Sec. V we study the performance of UNEDF1 with respect to global nuclear observables, spectroscopic properties, fission, and neutron droplets. Section VI contains the main conclusions and lays out future work.

II. THEORETICAL FRAMEWORK

A. Time-even Skyrme energy density functional

In the nuclear DFT, the total binding energy E of the nucleus is a functional of the one-body density ρ and pairing $\tilde{\rho}$ matrices. In its quasilocal approximation, it can be written as a three-dimensional (3D) spatial integral:

$$\begin{aligned} E[\rho,\tilde{\rho}] &= \int d^3\boldsymbol{r}\mathcal{H}(\boldsymbol{r}) \\ &= \int d^3\boldsymbol{r}\left[\mathcal{E}^{\mathrm{Kin}}(\boldsymbol{r})+\chi_0(\boldsymbol{r})+\chi_1(\boldsymbol{r})\right. \\ &\quad \left.+\tilde{\chi}(\boldsymbol{r})+\mathcal{E}^{\mathrm{Coul}}_{\mathrm{Dir}}(\boldsymbol{r})+\mathcal{E}^{\mathrm{Coul}}_{\mathrm{Exc}}(\boldsymbol{r})\right], \end{aligned} \tag{1}$$

where $\mathcal{H}(\boldsymbol{r})$ is the energy density that is quasilocal (it usually depends on derivatives with respect to the local densities), time-even, scalar, isoscalar, and real. It is usually broken down into the kinetic energy [$\mathcal{E}^{\mathrm{Kin}}(\boldsymbol{r})$] and nuclear potential [for both the particle-hole and particle-particle channels, $\chi_{0,1}(\boldsymbol{r})$ and $\tilde{\chi}(\boldsymbol{r})$, respectively] and Coulomb terms [$\mathcal{E}^{\mathrm{Coul}}_{\mathrm{Dir}}(\boldsymbol{r})$ and $\mathcal{E}^{\mathrm{Coul}}_{\mathrm{Exc}}(\boldsymbol{r})$]. For Skyrme functionals, the particle-hole energy density $\chi_0(\boldsymbol{r})+\chi_1(\boldsymbol{r})$ splits into $\chi_0(\boldsymbol{r})$, depending only on isoscalar densities, and $\chi_1(\boldsymbol{r})$, depending on isovector densities (and the isoscalar particle density through the density dependence of the coupling constant $C_1^{\rho\rho}$; see below) [4,32,33]. Each term takes the generic form,

$$\begin{aligned} \chi_t(\boldsymbol{r}) &= C_t^{\rho\rho}\rho_t^2+C_t^{\rho\tau}\rho_t\tau_t+C_t^{J^2}\boldsymbol{J}_t^2 \\ &\quad +C_t^{\rho\Delta\rho}\rho_t\Delta\rho_t+C_t^{\rho\nabla J}\rho_t\nabla\cdot\boldsymbol{J}_t, \end{aligned} \tag{2}$$

where ρ_t, τ_t, and $\boldsymbol{J}_t$ ($t=0,1$) can all be expressed in terms of full density matrix $\rho_t(\boldsymbol{r}\sigma,\boldsymbol{r}'\sigma')$; see Ref. [4] for details. (For brevity, we have omitted the explicit dependence of the densities on the coordinate $\boldsymbol{r}$.) The $\boldsymbol{J}_t$ density is the vector part of the spin-current density tensor $J_{\mu\nu}$. (As in our previous work [25], nonvector components of $J_{\mu\nu}$ were disregarded.) The coupling constants are real numbers, except for $C_t^{\rho\rho}$, which is taken to be density dependent:

$$C_t^{\rho\rho}=C_{t0}^{\rho\rho}+C_{t\mathrm{D}}^{\rho\rho}\rho_0^{\gamma}. \tag{3}$$

All volume coupling constants ($C_t^{\rho\rho}$ and $C_t^{\rho\tau}$) can be related to the constants characterizing the infinite nuclear matter [25], and this relation was used during the optimization to define the range of parameter changes.

The Coulomb contribution is treated as usual by assuming a point proton charge. The exchange term was computed at the Slater approximation:

$$\mathcal{E}^{\mathrm{Coul}}_{\mathrm{Exc}}(\boldsymbol{r})=-\frac{3}{4}e^2\left(\frac{3}{\pi}\right)^{1/3}\rho_{\mathrm{p}}^{4/3}. \tag{4}$$

For the pairing energy density $\tilde{\chi}(\boldsymbol{r})$, we use the mixed pairing description of Ref. [34] with

$$\tilde{\chi}(\boldsymbol{r})=\sum_{q=n,p}\frac{V_0^q}{2}\left[1-\frac{1}{2}\frac{\rho_0(\boldsymbol{r})}{\rho_{\mathrm{c}}}\right]\tilde{\rho}_q^2(\boldsymbol{r}), \tag{5}$$

where $\tilde{\rho}$ is the local pairing density. The value $\rho_c=0.16$ fm^{-3} is used throughout this paper. We allow for different pairing strengths for protons (V_0^p) and neutrons (V_0^n) [35]. A cutoff of $E_{\mathrm{cut}}=60$ MeV was used to truncate the quasiparticle space [36]. To prevent the collapse of pairing, we used the Lipkin-Nogami procedure according to Ref. [37].

B. Treatment of the center of mass

The success of the self-consistent mean-field theory is, to a great extent, because of the concept of symmetry breaking. A classic example is the breaking of the translational invariance by the mean field that is localized in space. The associated c.m. correction to the binding energy [4,38,39], $-\langle\hat{\boldsymbol{P}}^2_{\mathrm{c.m.}}\rangle/(2mA)$, is usually added to the DFT binding energy in Eq. (1). This correction contributes typically a few MeV to the total energy. Moreover, it was shown that adopting approximations to this correction during the optimization of the functional could lead to significantly different surface properties [4,17,40].

Because the c.m. correction is not additive in particle number, it causes serious conceptual problems when dealing with fission or heavy-ion fusion, that is, when one considers the split of the nucleus into several fragments, or formation of the compound nucleus through a merger of two lighter ions. In fission studies, it was shown that the contribution of the c.m. correction between the two prefragments could amount to several MeV near scission [41–43]. Moreover, properly computing this relative contribution is difficult, as it reflects the degree of entanglement between prefragments [43,44]. Time-dependent Hartree-Fock calculations of low-energy heavy-ion reactions are even more problematic, as there is currently no solution to the discontinuity of the c.m. correction between the target+projectile system and the compound nucleus [45,46]: Such calculations usually neglect the c.m. term altogether, even though EDFs employed in such calculations have been usually fitted with the c.m. correction included. There are, however, some exceptions (see, e.g., Ref. [47]). Note that the same problem occurs with the so-called rotational correction arising from the breaking of rotational invariance by deformed mean fields [41,48].

Another undesired property of the c.m. correction is that it slightly breaks the variational nature of HFB when adding or subtracting a particle [49] (i.e., it violates the Koopmans theorem). The resulting s.p. energy shifts are quite significant and they are of the order of the mass polarization effect related to the fact that when adding or subtracting a particle to a closed

spherical core, the resulting nucleus becomes deformed. If a spherical symmetry is imposed, the mass polarization effect is a self-consistent rearrangement of all nucleons, when an odd particle is introduced to the system. This corresponding energy shift is $E_{\rm Kin}/A^2$ (i.e., about 0.4 MeV in ^{40}Ca [49]).

As discussed in Sec. I, the EDF is supposed to capture all the physics of interest at the HFB level. In other words, the functional is to be built from the full single-reference density matrix. Although the HFB vacuum breaks the translational symmetry, the associated correction term should be absorbed in the density dependence. In particular, it should be possible to express the c.m. term not as an explicit function of A, as currently being done, but through a density functional. Until a simple prescription is proposed, however, it is more consistent to simply drop all corrections that originate from a Hamiltonian view of the problem, including the c.m. term. And, because our focus is on fission, this is precisely what we have done in this work.

III. OPTIMIZATION AND SENSITIVITY ANALYSIS

A. Experimental data set

Because the focus of this study is the construction of an EDF optimized for fission, our experimental data set was expanded by including the excitation energies (bandheads) of four fission isomers (FIs) listed in Table I. The ground-state (g.s.) binding energies of ^{238}U, ^{240}Pu, and ^{242}Cm, not included in the previous UNEDF0 data set [25], were added for consistency (the g.s. energy of ^{236}U was already there).

Consequently, compared with UNEDF0, the UNEDF1 data set contains seven new data points: three additional g.s. masses of deformed nuclei, and four excitation energies of FIs. For the FIs, we used the weight $w_i = 0.5$ MeV in the χ^2 objective function,

$$\chi^2(\mathbf{x}) = \sum_i \left(\frac{s_i(\mathbf{x}) - d_i}{w_i} \right)^2 . \tag{6}$$

The χ^2 weights for binding energies, proton rms radii, and odd-even mass (OEM) staggering are the same as in Ref. [25].

Two assumptions made in Ref. [25] were also adopted here: (i) Because the isovector effective mass cannot be reliably constrained by the current data, it was set to $1/M_v^* = 1.249$ as in UNEDF0 and the SLy4 parameterization [51], which was the initial starting point in our optimization; and (ii) because tensor terms are mostly sensitive to the single-particle (s.p.) shell structure, which is not directly constrained by the UNEDF1 data set, the tensor coupling constants $C_0^{J^2}$ and $C_1^{J^2}$ were set to zero.

TABLE I. Experimental excitation energies of fission isomers [50] (in MeV) considered in the UNEDF1 data set.

Z	N	E
92	144	2.750
92	146	2.557
94	146	2.800
96	146	1.900

In summary, compared with UNEDF0 [25], the optimization of UNEDF1 is characterized by the following:

(i) The same 12 EDF parameters to be optimized, namely, ρ_c, $E^{\rm NM}/A$, $K^{\rm NM}$, $a_{\rm sym}^{\rm NM}$, $L_{\rm sym}^{\rm NM}$, M_s^*, $C_0^{\rho\Delta\rho}$, $C_1^{\rho\Delta\rho}$, V_0^n, V_0^p, $C_0^{\rho\nabla J}$, and $C_1^{\rho\nabla J}$;
(ii) Seven additional data points: three new masses and four FI energies with the weights $w = 0.5$ MeV;
(iii) Neglect of the c.m. correction term.

B. Numerical precision and implementation

All HFB calculations were run with the code HFBTHO [52]. The code expands the HFB solutions on the axially symmetric, deformed harmonic oscillator (HO) basis. In the optimization of UNEDF0, we used a spherical basis with 20 HO shells, which was found to give a good compromise between the numerical precision and computational performance. The current optimization includes states with much larger deformation than in the ground state, and the dependence of the energies with respect to the set of basis states is more significant.

In the UNEDF1 optimization, all quantities but the four fission isomers were computed with the spherical HO basis of $N_{\rm sh} = 20$ shells, which includes $N = 1771$ basis states. For the fission isomers, we adopted a stretched HO basis with deformation $\beta = 0.4$. The basis contains up to $N_{\rm sh} = 50$ oscillator shells with an upper limit of $N = 1771$ basis states with lowest HO s.p. energies. The oscillator frequency $\omega_0^3 = \omega_\perp^2 \omega_\parallel$ was set at $\hbar\omega_0 = 1.2 \times 41/A^{1/3}$ MeV. As seen in Fig. 1, at this selection of the HO basis, the dependence of FI energies on the basis deformation remains fairly constant around $\beta = 0.4$. Moreover, the range of variations is significantly less than the corresponding χ^2 weight, $w_i = 0.5$ MeV.

Optimization calculations were performed on Argonne National Laboratory's Fusion cluster, managed by Argonne's Laboratory Computing Resource Center (LCRC). Fusion consists of 320 computing nodes, each with dual quad-core Pentium Xeon processors. By using Intel's Math Kernel Library and the Intel Fortran compiler (ifort), we were able to

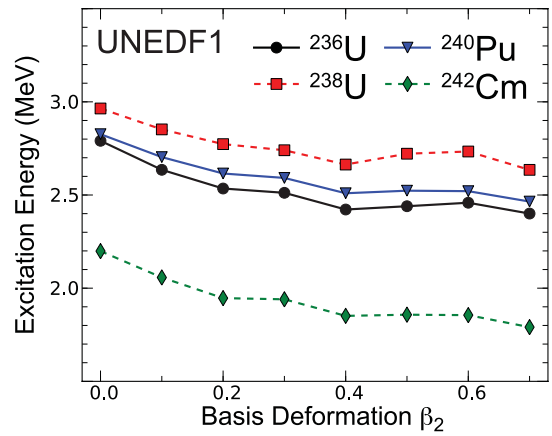

FIG. 1. (Color online) Excitation energies of fission isomers considered in the UNEDF1 optimization as functions of the HO basis deformation.

run HFBTHO in almost half the time when compared with the prebuilt reference BLAS library implementation and GNU's gfortran compiler. We were also able to dramatically reduce the wall-clock time of an HFBTHO computation by using OpenMP at the node level to parallelize key computational bottlenecks. These bottlenecks involved iteratively computing the eigenvalues and eigenvectors of the (Ω, π) blocks of the HFB matrix, as well as the density calculations reflecting the same block pattern. OpenMP allowed us to dynamically assign processors to blocks of data for parallel processing, which further reduced the wall-clock time by a factor of 6 when running on an eight-core node.

The parameter estimation computations presented in this paper ran 218 total simulations of HFBTHO for each nucleus in the data set, using 80 compute nodes (640 cores) for 5.67 h. As highlighted in Ref. [25], using the POUNDerS algorithm [Practical Optimization Using No Derivatives (for Squares)] on the type of fitting problem considered here requires more than 10 times fewer HFBTHO runs over a more traditional, derivative-free Nelder-Mead optimization method [53]. Hence, without the algorithmic and computational advancements detailed above, a similar optimization could have previously consumed a month of computations using 80 cores of the Fusion cluster.

We emphasize that, strictly speaking, both the UNEDF0 and the UNEDF1 parameterizations obtained in this work should always be used in their original environment. In particular, the pairing EDF should be that of Eq. (5) used with the original pairing space cutoff; pairing calculations must be complemented by the Lipkin-Nogami prescription; and the proton and neutron pairing strengths must not vary from the values determined by our optimization. In short, contrary to usual practice, there is no flexibility in the treatment of the pairing channel.

C. Result of the optimization: UNEDF1 parameter set

The starting point for our POUNDerS optimization was the previously obtained UNEDF0 parameterization. After 177 simulations, the algorithm reached the new optimal result. The resulting parameter set is listed in Table II. The first six parameters were restricted to lie within finite bounds, also listed in Table II, that were not allowed to be violated during the optimization procedure. As can be seen, parameters $E^{\rm NM}/A$ and $K^{\rm NM}$ are on the boundary value. In the case of UNEDF0, we recall that $K^{\rm NM}$ and $1/M_s^*$ also ended up at their respective boundaries. The saturation density ρ_c is given with more digits than the other parameters. Such extra precision is needed when computing volume coupling constants [25].

We first note that the same minimum was obtained by starting either from the UNEDF0 solution or from the UNEDF1ex parameterization discussed below: This gives us confidence that the parameter set listed in Table II is sufficiently robust. We can then observe that most of the parameter values of UNEDF1 are fairly close to those of UNEDF0 [25]. There are, nevertheless, a couple of notable exceptions. First, the magnitude of $C_1^{\rho\Delta\rho}$ is now much larger. This is potentially dangerous, as it might trigger scalar-isovector instabilities in the functional that could appear in neutron-rich nuclei [54,55]. (Our mass-table calculations with UNEDF1 do not show indications of instability in even-even nuclei.) Second, $C_1^{\rho\nabla J}$ has drifted considerably from its initial value, even changing sign. These two coupling constants control the isovector surface properties of the nucleus; hence, only proper constraints on the shell structure like, for example, spin-orbit splitting in neutron-rich nuclei will allow these terms to be pinned down. For the moment, both coupling constants are relatively unconstrained, as evidenced also by their relatively large σ value shown in Table II.

D. Sensitivity analysis

1. *Correlation matrix of* UNEDF1

We have performed a sensitivity analysis at the solution of the optimization. All residual derivatives were estimated by using the optimal finite-difference procedure detailed in Ref. [56]. Because some of the parameters ran at their bounds during the optimization, the sensitivity analysis was carried out in a subspace that does not contain these parameters.

TABLE II. Optimized parameter set UNEDF1. Listed are bounds used in the optimization, final optimized parameter values, standard deviations, and 95% confidence intervals.

x	Bounds	$\hat{\mathbf{x}}^{(\rm fin.)}$	σ	95% CI
$\rho_{\rm c}$	[0.15,0.17]	0.15871	0.00042	[0.158, 0.159]
$E^{\rm NM}/A$	[−16.2,−15.8]	−15.800	—	—
$K^{\rm NM}$	[220, 260]	220.000	—	—
$a_{\rm sym}^{\rm NM}$	[28, 36]	28.987	0.604	[28.152, 29.822]
$L_{\rm sym}^{\rm NM}$	[40, 100]	40.005	13.136	[21.841, 58.168]
$1/M_s^*$	[0.9, 1.5]	0.992	0.123	[0.823, 1.162]
$C_0^{\rho\Delta\rho}$	[−∞, +∞]	−45.135	5.361	[−52.548, −37.722]
$C_1^{\rho\Delta\rho}$	[−∞, +∞]	−145.382	52.169	[−217.515, −73.250]
V_0^n	[−∞, +∞]	−186.065	18.516	[−211.666, −160.464]
V_0^p	[−∞, +∞]	−206.580	13.049	[−224.622, −188.538]
$C_0^{\rho\nabla J}$	[−∞, +∞]	−74.026	5.048	[−81.006, −67.046]
$C_1^{\rho\nabla J}$	[−∞, +∞]	−35.658	23.147	[−67.663, −3.654]

TABLE III. Correlation matrix for UNEDF1 parameter set. Correlations greater than 0.8 (in absolute value) are in boldface.

ρ_c	1.00									
$a_{\rm sym}^{\rm NM}$	−0.35	1.00								
$L_{\rm sym}^{\rm NM}$	−0.14	0.71	1.00							
$1/M_s^*$	0.32	0.23	0.36	1.00						
$C_0^{\rho\Delta\rho}$	−0.25	−0.25	−0.35	−0.99	1.00					
$C_1^{\rho\Delta\rho}$	−0.06	−0.15	−0.77	−0.22	0.19	1.00				
V_0^n	−0.32	−0.22	−0.36	−0.99	**0.98**	0.22	1.00			
V_0^p	−0.33	−0.18	−0.29	−0.97	**0.97**	0.15	**0.96**	1.00		
$C_0^{\rho\nabla J}$	−0.14	−0.20	−0.32	−0.86	**0.91**	0.22	**0.85**	**0.84**	1.00	
$C_1^{\rho\nabla J}$	0.05	−0.17	−0.13	−0.10	0.07	0.21	0.10	0.07	−0.03	1.00
	ρ_c	$a_{\rm sym}^{\rm NM}$	$L_{\rm sym}^{\rm NM}$	$1/M_s^*$	$C_0^{\rho\Delta\rho}$	$C_1^{\rho\Delta\rho}$	V_0^n	V_0^p	$C_0^{\rho\nabla J}$	$C_1^{\rho\nabla J}$

The same strategy was also used in the previous sensitivity analysis of the UNEDF0 parameterization; we refer to Ref. [25] for a detailed discussion of the available options in the case of constrained optimization. In Table II we list the standard deviation σ and 95% confidence interval (CI) for each parameter at the solution. As discussed in Sec. III C, the standard deviations of most of the parameters is relatively small.

The correlation matrix for the UNEDF1 parameter set is presented in Table III. It was calculated as in Ref. [25] and, similarly, corresponds to the 10-dimensional subspace of the parameters that are not at their boundary value. Generally, most of the parameters are only slightly correlated to each other, with a few notable exceptions (correlations below 0.8 are not very significant from a statistical viewpoint). The strong correlation between $1/M_s^*$ and both V_0^n and V_0^p had already been noticed in the UNEDFnb parameter set of Ref. [25] and reflects the interplay between the level density at the Fermi surface and the size of pairing correlations. Similarly, both pairing strengths are strongly correlated with $C_0^{\rho\Delta\rho}$, which can also be related to surface properties of the functional. Interestingly, both pairing strengths are now strongly correlated with one another, which was not the case with UNEDF0. The same correlation matrix of Table III is shown graphically in Fig. 2.

Next, we study the overall impact of each data type in our χ^2 function on the obtained parameter set. As in Ref. [25] we calculate the partial sums of the sensitivity matrix for each data type. Let us recall that the sensitivity matrix S is defined as

$$S(\mathbf{x}) = [J(\mathbf{x})J^{\rm T}(\mathbf{x})]^{-1}J(\mathbf{x})\,, \tag{7}$$

where $J(\mathbf{x})$ is the Jacobian matrix. The results are illustrated in Fig. 3, where we have summed absolute values of each data type for each parameter. The total strengths for each parameter were then normalized to 100%. Note that the fission isomer excitation energies represent less than 4% of the total number of data points but account for typically 30% of the variation of the parameter set. In the case of the symmetry energy coefficient, this percentage is even 75% (see Sec. IV for more discussion). Compared with UNEDF0, we find that the overall dependence on the proton radii has significantly decreased, except for ρ and $C_1^{\rho\Delta\rho}$, and that the dependence on the OES has actually increased. This kind of analysis, however, does not address the importance of a particular data point to the obtained optimal solution.

A complementary way to study the impact of an individual datum on the obtained parameter set is therefore presented in Fig. 4. Here, we have plotted the amount of variation,

$$||\delta\mathbf{x}/\sigma|| = \sqrt{\sum_k \left(\frac{\delta x_k}{\sigma}\right)^2}\,, \tag{8}$$

for the optimal parameter set when data points d_i are changed by an amount of $0.1w_i$ one by one. As can be seen, the variations are small overall, assuring us that the data set was chosen correctly. The masses of the double magic nuclei ^{208}Pb and ^{58}Ni seem to have the biggest relative impact on the optimal parameter set. One can also see that the sensitivity of the parameters on the new FI data is larger than the average datum point. By contrast, the dependence of the parameterization on the masses of deformed actinide and rare earth nuclei is weaker.

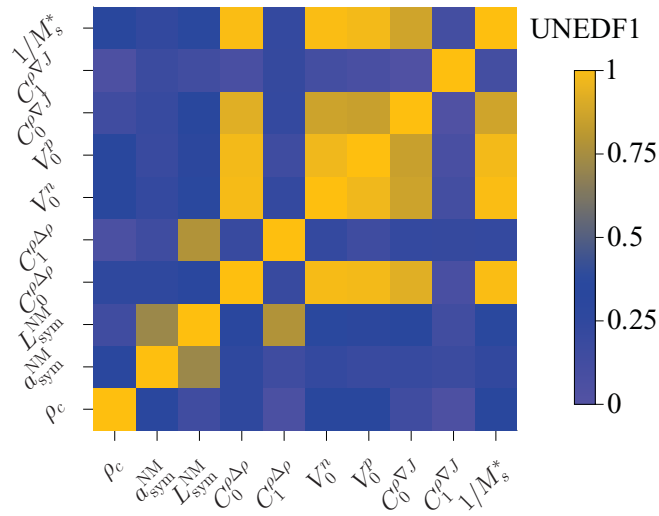

FIG. 2. (Color online) Absolute values of the correlation matrix of Table III presented in a color-coded format.

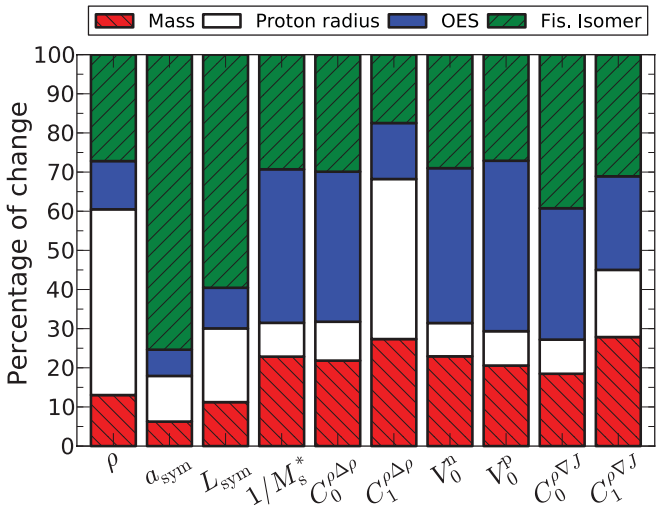

FIG. 3. (Color online) Sensitivity of UNEDF1 to different types of data entering the χ^2 function.

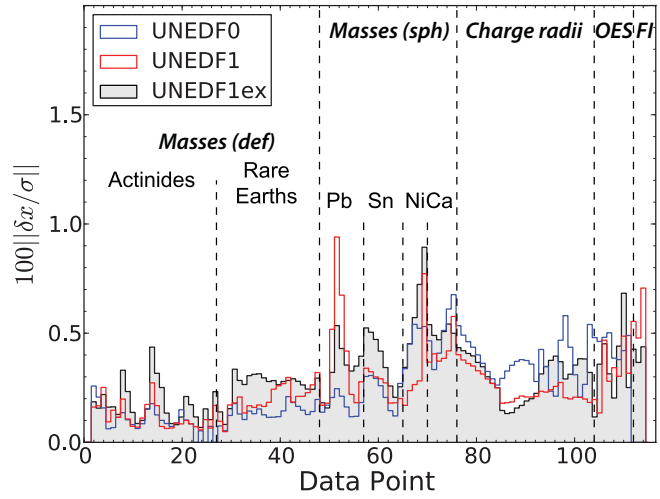

FIG. 4. (Color online) Overall change in **x** for the UNEDF1 when the datum d_i is changed by an amount of $0.1w_i$ one by one. The four rightmost data points marked FI correspond to excitation energies of fission isomers. The results for UNEDF0 and UNEDF1ex of Sec. III D2 are also shown.

2. *Discussion of the Coulomb exchange term*

It was argued in Ref. [57] that removing the Coulomb exchange term from the functional could improve the overall fit on nuclear binding energies. This procedure had been motivated by the earlier works, Refs. [58,59], in which similar ameliorations, albeit on a smaller data set, were observed. The origin of these ad hoc manipulations was the observation that many-body effects induced by the long-range Coulomb force among protons manifest themselves in the form of a (positive) correlation energy, which, to some extent, can cancel out the (negative) exchange term [60,61]. Because such an exchange-correlation effect is absent from the standard Skyrme functional, one could feel justified to simulate it by effectively screening the Coulomb exchange term with an empirical factor $0 \leqslant \alpha_{\rm ex} \leqslant 1$. The special cases $\alpha_{\rm ex} = 0$ and $\alpha_{\rm ex} = 1$ give, respectively, the case without and with full Coulomb exchange.

The result of the optimization of the functional with this additional parameter $\alpha_{\rm ex}$ is given in Table IV. Our objective function is slightly decreased from 51.058 to 49.341 when this term is present. Overall, both parameterizations, with and without the Coulomb exchange screening term, are very similar. However, one can see that the 95% CI is relatively large for the screening parameter, the value of which is also close to 1 (full Coulomb exchange). We recall that this confidence interval is extracted from the correlation matrix computed in the 10-D space of "inactive" parameters, namely, the space of the 10 parameters that are not at their bound and thus actively constrained. If one computes the Jacobian matrix in the original 13-D space of all parameters with a tangent plane approximation to account for the three active parameters $E^{\rm NM}$, $K^{\rm NM}$, and $L^{\rm NM}_{\rm sym}$, we find that the 95% CI for the screening parameter becomes $[-1.663, 3.290]$. This implies that $\alpha_{\rm ex}$ is basically not constrained with the current data set.

TABLE IV. Optimized parameter set UNEDF1ex. Listed are bounds used in the optimization, final optimized parameters, standard deviations, and 95% confidence intervals.

x	Bounds	$\hat{\mathbf{x}}^{(\rm fin.)}$	σ	95% CI
$\rho_{\rm c}$	[0.15, 0.17]	0.15837	0.00049	[0.158, 0.159]
$E^{\rm NM}/A$	$[-16.2, -15.8]$	-15.800	—	—
$K^{\rm NM}$	[220, 260]	220.000	—	–
$a^{\rm NM}_{\rm sym}$	[28, 36]	28.384	0.711	[27.417, 29.351]
$L^{\rm NM}_{\rm sym}$	[40, 100]	40.000	—	—
$1/M^*_s$	[0.9, 1.5]	1.002	0.123	[0.835, 1.169]
$C_0^{\rho\Delta\rho}$	$[-\infty, +\infty]$	-44.602	5.349	$[-51.872, -37.331]$
$C_1^{\rho\Delta\rho}$	$[-\infty, +\infty]$	-180.956	47.890	$[-246.050, -115.863]$
V_0^n	$[-\infty, +\infty]$	-187.469	18.525	$[-212.649, -162.288]$
V_0^p	$[-\infty, +\infty]$	-207.209	13.106	$[-225.024, -189.395]$
$C_0^{\rho\nabla J}$	$[-\infty, +\infty]$	-74.339	5.187	$[-81.389, -67.289]$
$C_1^{\rho\nabla J}$	$[-\infty, +\infty]$	-38.837	23.435	$[-70.690, -6.984]$
$\alpha_{\rm ex}$	[0, 1]	0.813	0.154	[0.604, 1.023]

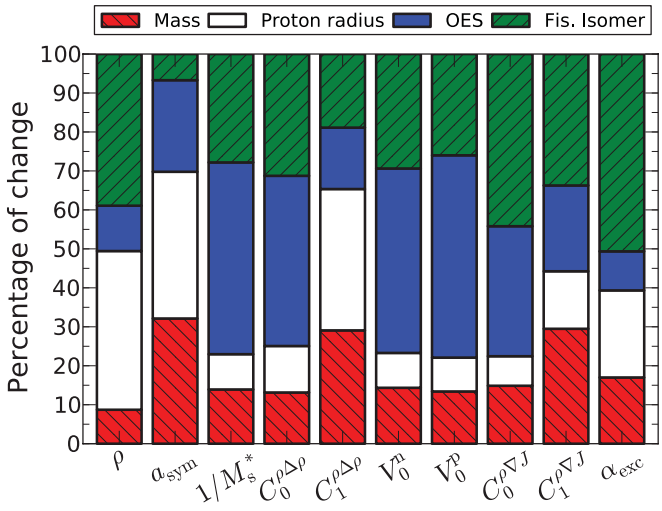

FIG. 5. (Color online) Similar as in Fig. 3 but for the UNEDF1ex parameter set.

The dependence of every parameter on the four types of data included in the data set (masses, charge radii, OES, and FI data) reveal an interesting consequence of the screening of the Coulomb exchange term. Figure 5 shows the analog of Fig. 3 when the screening parameter α_{ex} is included. Note the striking difference in the bar plot for the symmetry energy parameter a_{sym}^{NM}: Fluctuations in this parameter under a variation of the excitation energy of the fission isomers are reduced to less than 10%, compared with nearly 75% when the full Coulomb exchange term is computed.

This behavior can be qualitatively understood by recalling a few simple facts about the bulk nuclear energy and deformation. A variation of the excitation energy of very deformed states such as fission isomers essentially affects the bulk surface properties of the functional—especially if the coupling constants driving shell effects are somewhat constrained by the data set. In the language of the leptodermous expansion of Sec. IV C, this implies that both the surface and surface-symmetry energy coefficients (which depend in a nontrivial way on the coupling constants of the functional) should be impacted. On the other hand, we may assume that the isospin dependence of the binding energy (i.e., the total symmetry energy) is relatively well constrained by the several long isotopic sequences present in our data set. We therefore see that the requirement of having the full symmetry energy constrained together with a relatively large variation of the surface terms should lead to a relatively large variation of the volume symmetry a_{sym}^{NM}, which is indeed observed in Fig. 4.

One can now understand the difference of behavior of a_{sym}^{NM} under a change of data when the Coulomb screening term is present: According to [60,61], the many-body Coulomb correlation energy that is simulated by $\alpha_{ex} < 1$ essentially represents a proton surface effect. Changes in bulk surface properties triggered by variations in the excitation energy of fission isomers can be entirely absorbed by a readjustment of α_{ex}, especially because the latter is poorly constrained by the other data, rather than by a_{sym}^{NM}. Lastly, we note that the Coulomb exchange term, which is approximated by the usual local Slater expression, may get worse at large deformations [62].

In summary, considering that (i) α_{ex} is poorly constrained by the data, yet may affect significantly other parameters like a_{sym}^{NM} and (ii) α_{ex} does not significantly improve the quality of the fit, we decided to retain the full Coulomb exchange term in the present UNEDF1 parameterization.

IV. CHARACTERIZATION OF UNEDF1 PARAMETERIZATION

In this section, we discuss general properties of the UNEDF1 parameterization and compare it with UNEDF0.

A. Energy density in (t, x) parameterization

For practical applications, it is useful to express the coupling constants of UNEDF0 and UNEDF1 in the traditional (t, x) parameterization of the standard Skyrme force (see Appendix A of [4]). The results are given in Table V.

As can be seen, in the (t, x) parameterization the two functionals are quite different. This is to be expected as the relation between the C and (t, x) parameterizations is partially nonlinear [63].

B. Energy density parameters in natural units

The EDF parameters can also be expressed in terms of natural units [63]. In Table VI we list the parameter set of UNEDF1 in standard units and in natural units. Here we have used the same value for the scale $\Lambda = 687$ MeV, characterizing the breakdown of the chiral effective theory, which was found in Ref. [63]. From the numbers in Table VI one can see that most of the UNEDF1 parameters are natural, with only two minor exceptions. First, because the effective mass M_s^* in our optimum is close to unity, the $C_0^{\rho\tau}$ is abnormally small. Second, $C_1^{\rho\Delta\rho}$ seems to be on the borderline of being unnaturally large. As Table II indicates, however, the standard deviation for this parameter is rather large. It has to be noted, however, that there is nothing unusual about the magnitude of $C_1^{\rho\Delta\rho}$. Indeed, some

TABLE V. Parameters (t, x) of UNEDF0 and UNEDF1.

Parameters	UNEDF0	UNEDF1	Units
t_0	−1883.68781034	−2078.32802326	MeV·fm^3
t_1	277.50021224	239.40081204	MeV·fm^5
t_2	608.43090559	1575.11954190	MeV·fm^5
t_3	13901.94834463	14263.64624708	MeV·fm$^{3+3\gamma}$
x_0	0.00974375	0.05375692	—
x_1	−1.77784395	−5.07723238	—
x_2	−1.67699035	−1.36650561	—
x_3	−0.38079041	−0.16249117	—
b_4	125.16100000	38.36807206	MeV·fm^5
b_4'	−91.2604000	71.31652223	MeV·fm^5
γ	0.32195599	0.27001801	—

TABLE VI. Coupling constants of UNEDF0 and UNEDF1 in normal units and in natural units. Value $\Lambda = 687$ MeV was used.

Coupling constant	UNEDF0		UNEDF1	
	Normal units	Natural units	Normal units	Natural units
$C_{00}^{\rho\rho}$	−706.38	−0.795	−779.37	−0.878
$C_{10}^{\rho\rho}$	240.26	0.271	288.01	0.324
$C_{0D}^{\rho\rho}$	868.87	0.901	891.48	0.937
$C_{1D}^{\rho\rho}$	−69.77	−0.072	−201.37	−0.212
$C_{0}^{\rho\tau}$	−12.92	−0.176	−0.99	−0.014
$C_{1}^{\rho\tau}$	−45.08	−0.616	−33.52	−0.458
$C_{0}^{\rho\Delta\rho}$	−55.26	−0.755	−45.14	−0.616
$C_{1}^{\rho\Delta\rho}$	−55.62	−0.759	−145.38	−1.985
$C_{0}^{\rho\nabla J}$	−79.53	−1.086	−74.03	−1.011
$C_{1}^{\rho\nabla J}$	45.63	0.623	−35.66	−0.487
γ	0.3220		0.2700	

examples of EDF parameterizations with similar or larger values of $C_1^{\rho\Delta\rho}$ can be found in Fig. 2 of [63].

C. Leptodermous expansion

To extract global properties of the energy functional and relate them to the familiar constants of the liquid drop model (LDM), one needs to carry out the leptodermous expansion. The general strategy behind the expansion of nuclear EDF was discussed in Ref. [64], where one can find the relevant literature on this topic. The starting point is the LDM binding energy per nucleon expanded in the inverse radius ($\propto A^{-1/3}$) and neutron excess $I = (N - Z)/A$:

$$\mathcal{E}(A, I) = a_{\rm vol} + a_{\rm surf}A^{-1/3} + a_{\rm curv}A^{-2/3} + a_{\rm sym}I^2 + a_{\rm ssym}A^{-1/3}I^2 + a_{\rm sym}^{(2)}I^4. \quad (9)$$

For any functional, our approach consists of combining nuclear matter (NM) calculations with Hartree-Fock (HF) calculations for a large set of spherical nuclei to extract by linear regression the various parameters of the expansion (9) according to the following procedure.

First, the bulk parameters $a_{\rm vol}$ and $a_{\rm sym}$ are directly obtained from NM calculations. Second, the smooth energy per nucleon $\bar{\mathcal{E}}(A, I)$ is extracted from the spherical HF calculations of (A, I) nuclei by removing the shell correction [64]. The isoscalar coefficients of the expansion (9) can then be deduced from the smooth energy by plotting

$$[\bar{\mathcal{E}}(A, 0) - a_{\rm vol}]A^{1/3} \longrightarrow a_{\rm surf} + a_{\rm curv}A^{-1/3} \quad (10)$$

as a function of $A^{-1/3}$. The $a_{\rm surf}$ coefficient is obtained as the extrapolation of the curve to $A^{-1/3} \longrightarrow 0$. The curvature coefficient $a_{\rm curv}$ is then estimated from the slope of the line.

The determination of isovector coefficients starts with the second-order symmetry coefficient $a_{\rm sym}^{(2)}$. It is easily estimated by systematic calculations in asymmetric NM. Defining

$$a_{\rm sym}^{\rm (eff)}(\infty, I) = [\mathcal{E}^{\rm NM}(\infty, I) - \mathcal{E}^{\rm NM}(\infty, 0)]/I^2 \longrightarrow a_{\rm sym} + a_{\rm sym}^{(2)}I^2, \quad (11)$$

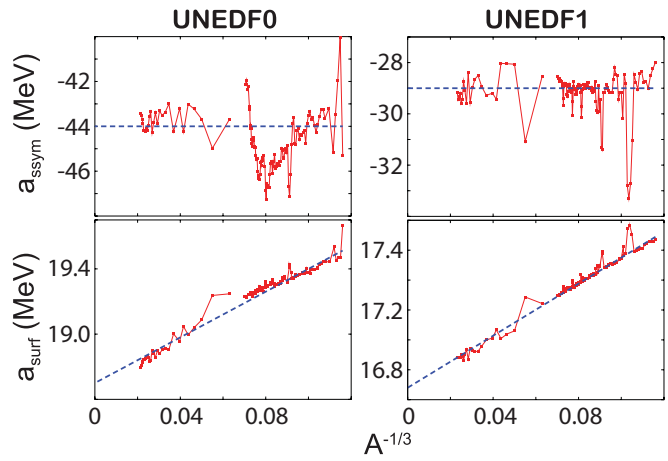

FIG. 6. (Color online) Surface-symmetry coefficient (15) (upper panels) and surface coefficient (lower panels) versus $A^{-1/3}$ for UNEDF0 (left) and UNEDF1 (right).

one can extract the second-order symmetry coefficient from the slope of $a_{\rm sym}^{\rm (eff)}(\infty, I)$ versus I^2. Extracting the surface-symmetry coefficient is more involved. We first introduce the effective symmetry coefficient for a finite nucleus as

$$a_{\rm sym}^{\rm (eff)}(A, I) = [\bar{\mathcal{E}}(A, I) - \bar{\mathcal{E}}(A, 0)]/I^2 \longrightarrow a_{\rm sym} + a_{\rm ssym}A^{-1/3} + a_{\rm sym}^{(2)}I^2. \quad (12)$$

In nuclear matter ($A \to +\infty$), the effective symmetry coefficient reduces to (11). To avoid multidimensional regression analysis, we introduce the reduced symmetry coefficient by subtracting the I^2-dependent part of the NM limit to $a_{\rm sym}^{\rm (eff)}$:

$$a_{\rm sym}^{\rm (red)}(A, I) = [\bar{\mathcal{E}}(A, I) - \bar{\mathcal{E}}(A, 0)]/I^2 - a_{\rm sym}^{(2)}I^2. \quad (13)$$

At the perfect LDM limit, the quantity $a_{\rm sym}^{\rm (red)}(A, I)$ should not depend on the neutron excess. At small isospins, however, numerical uncertainties in the shell-correction procedure are amplified by the I^2 denominator. In practice, it is more efficient to build an I-averaged reduced asymmetry coefficient,

$$\overline{a_{\rm sym}^{\rm (red)}} = \frac{1}{b-a}\int_a^b dI\, a_{\rm sym}^{\rm (red)}(A, I), \quad (14)$$

where we choose $a = 0.1$ and $b = 0.2$ [64]. The surface-symmetry energy is then obtained from

$$\left[\overline{a_{\rm sym}^{\rm (red)}} - a_{\rm sym}\right]A^{1/3} = a_{\rm ssym}. \quad (15)$$

Figure 6 illustrates the numerical accuracy of the method of evaluation for the surface and surface-symmetry coefficients of the LDM. The dashed blue lines indicate the fitting lines from which the final values of $a_{\rm surf}$, $a_{\rm curv}$, and $a_{\rm ssym}$ are deduced. The case of UNEDF1 seems to be clear. The trend of the surface energy for UNEDF0 is less clean. The two groups of nuclei, huge and large, seem to follow slightly different slopes, and the fit represents a compromise. The resulting surface and curvature energy have to be taken with care.

The LDM parameters of UNEDF0 and UNEDF1 are given in Table VII. As seen in Table I of Ref. [64] and Fig. 1 of Ref. [26], symmetry coefficients of phenomenological LDM mass models cluster around $a_{\rm sym} = 30$ MeV and

TABLE VII. Liquid drop coefficients of UNEDF0 and UNEDF1 (all in MeV).

	$a_{\rm vol}$	$a_{\rm sym}$	$a^{(2)}_{\rm sym}$	$a_{\rm surf}$	$a_{\rm curv}$	$a_{\rm ssym}$
UNEDF0	−16.056	30.543	4.418	18.7	7.1	−44
UNEDF1	−15.800	28.987	3.637	16.7	8.8	−29

$a_{\rm ssym} = -45$ MeV, and the UNEDF0 values are right in the middle. This result is not surprising, as this EDF was optimized primarily to nuclear masses. Indeed, the main difference between UNEDF0 and UNEDF1 lies in surface properties. Relatively low values of $a_{\rm surf}$ and $a_{\rm ssym}$ of UNEDF1 reflect the new constraints on the FI data and the neglect of the c.m. term. Again, comparing the LDM values of UNEDF1 with those in Table I of Ref. [64], we note that the LDM parameters of UNEDF1 are closest to those of the BSk6 EDF [65] ($a_{\rm surf} =$ 17.3 MeV and $a_{\rm ssym} = -33$ MeV) and the LSD LDM [66] ($a_{\rm surf} = 17.0$ MeV and $a_{\rm ssym} = -38.9$ MeV). In Sec. V C, we shall see that the reduced surface energy of UNEDF1 with respect to UNEDF0 has profound consequences for the description of fission barriers in the actinides. To see this reduction more clearly, we inspect the effective surface coefficient,

$$a^{(\rm eff)}_{\rm surf} = a_{\rm surf} + a_{\rm ssym} I^2. \tag{16}$$

For ^{240}Pu, the value of $a^{(\rm eff)}_{\rm surf}$ is 15.33 MeV for UNEDF1, 16.63 MeV for UNEDF0, 15.87 MeV for SLy4, 15.75 MeV for BSk6, 15.15 MeV for SkM*, and 15.17 MeV for LSD.

V. PERFORMANCE OF UNEDF1

A. Global mass table

One of the key elements required from the universal EDF is the ability to predict global nuclear properties, such as masses, radii, and deformations, across the nuclear chart, from drip line to drip line. We have calculated the g.s. mass table with UNEDF1 for even-even nuclei with $N, Z > 8$. Table VIII contains the rms deviations from experiment for binding energies, separation energies, averaged three-point odd-even mass differences, and proton radii. Because the set of fit observables constraining UNEDF1 is biased toward heavy nuclei, we also show rms deviations for light ($A < 80$) and heavy ($A \geqslant 80$) subsets.

Figure 7 displays the binding energy residuals (i.e., deviations from experiment). From this figure and Table VIII, we can see a couple of trends. First, the energy residuals with UNEDF1 are larger than those for UNEDF0. This result is not surprising, as the new data on FI and the removal of the center-of-mass correction strongly disfavors the lightest nuclei during the optimization process. Second, the characteristic arclike behavior between the magic numbers is pronounced, although this trend is much weaker than, for example, for the SLy4 functional (see Fig. 7 of Ref. [25]).

In Fig. 8 we display the residuals of two-neutron and two-proton separation energies. Again, the emphasis of UNEDF1 on heavy nuclei is clearly seen, and the corresponding rms deviations in Table VIII quantify this feature. Notice that two-

TABLE VIII. Root-mean-square deviations from the experimental values for UNEDF0 and UNEDF1 for different observables calculated in even-even systems: binding energy E, two-neutron separation energy S_{2n}, two-proton separation energy S_{2p}, three-point odd-even mass difference $\tilde{\Delta}^{(3)}_n$ (all in MeV), and rms proton radii $R_{\rm p}$ (in fm). Columns are observable, RMS deviation for UNEDF0 and UNEDF1, and the number of data points.

Observable	UNEDF0	UNEDF1	No.
E	1.428	1.912	555
E ($A < 80$)	2.092	2.566	113
E ($A \geqslant 80$)	1.200	1.705	442
S_{2n}	0.758	0.752	500
S_{2n} ($A < 80$)	1.447	1.161	99
S_{2n} ($A \geqslant 80$)	0.446	0.609	401
S_{2p}	0.862	0.791	477
S_{2p} ($A < 80$)	1.496	1.264	96
S_{2p} ($A \geqslant 80$)	0.605	0.618	381
$\tilde{\Delta}^{(3)}_n$	0.355	0.358	442
$\tilde{\Delta}^{(3)}_n$ ($A < 80$)	0.401	0.388	89
$\tilde{\Delta}^{(3)}_n$ ($A \geqslant 80$)	0.342	0.350	353
$\tilde{\Delta}^{(3)}_p$	0.258	0.261	395
$\tilde{\Delta}^{(3)}_p$ ($A < 80$)	0.346	0.304	83
$\tilde{\Delta}^{(3)}_p$ ($A \geqslant 80$)	0.229	0.248	312
$R_{\rm p}$	0.017	0.017	49
$R_{\rm p}$ ($A < 80$)	0.022	0.019	16
$R_{\rm p}$ ($A \geqslant 80$)	0.013	0.015	33

proton separation energies are systematically overestimated. The same trend is observed for the UNEDF0 functional. We can speculate about sources for this effect: (i) Following the arguments of Ref. [60], one may argue that the standard Skyrme functionals, such as UNEDF0 and UNEDF1, lack the capability to describe many-body Coulomb effects; (ii) the explicit contribution of the Coulomb field to the pairing channel [67,68] is not taken into account. It is expected that separate pairing strengths for neutrons and protons, as in UNEDF1, will partly account for this missing contribution [35]. However, the existence of nontrivial correlations between pairing strengths and other parameters of the functional (see

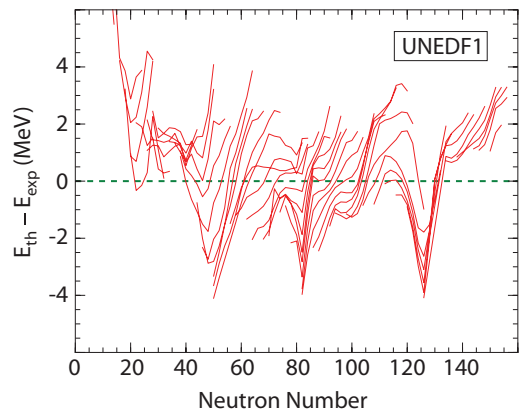

FIG. 7. (Color online) Binding energy residuals between UNEDF1 results and experiment for 555 even-even nuclei. Isotopic chains of a given element are connected by lines.

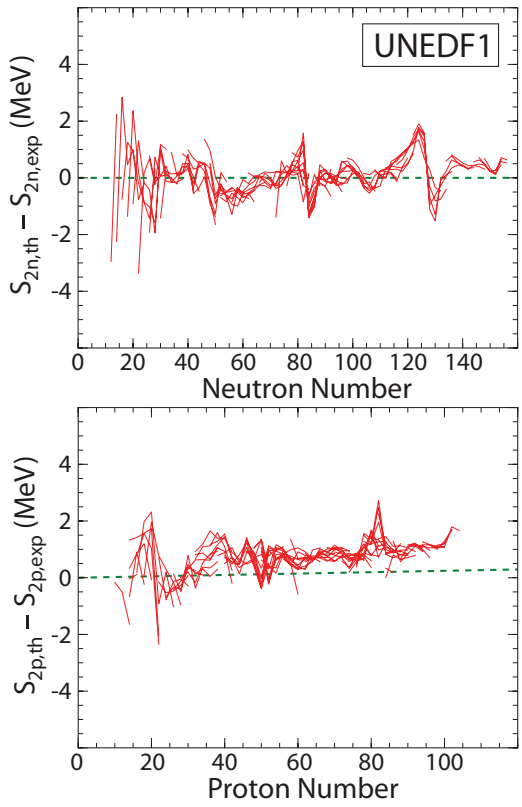

FIG. 8. (Color online) Two-neutron (top) and two-proton (bottom) separation energy residuals between UNEDF1 results and experiment.

Table III) may have consequences for observables such as two-proton separation energies.

To compare UNEDF0 and UNEDF1 quantitatively, we can assess their performance on various observables listed in Table VIII. It is expected that because new constraints on fission isomers have been added when optimizing UNEDF1 while keeping the same number of parameters optimized, the rms deviations for masses and separation energies must increase. Indeed, the rms deviation for the masses is slightly worse for UNEDF1, for both light and heavy nuclei. Interestingly, the quality of S_{2n} values remains roughly the same in both cases, as is true also for odd-even mass differences and proton radii.

B. Spherical shell structure

The nuclear shell structure has a substantial impact on many nuclear properties. Notably, the single-particle levels close to the Fermi surface affect many nuclear properties such as the strength of pairing correlations and deformability. Compared with our previous work [25], the s.p. energies that we report here have been obtained from proper blocking calculations at the HFB + LN level [69], instead of being the eigenvalues of the HF Hamiltonian. This choice is motivated by the need to stay within a logically consistent framework: Both UNEDF0 and UNEDF1 have been optimized at the HFB + LN level, and hence should be employed exclusively in this context. Moreover, in the nuclear mean-field theory with effective interactions, HF eigenvalues are a poor representation of s.p. energies; see [70,71] for a recent study. In a DFT approach, however, it is assumed that the generalized form of the energy density may effectively account for beyond mean-field effects such as particle-vibration couplings. In addition to this theoretical argument, let us recall that s.p. energies are not observables but model-dependent quantities extracted experimentally from binding energies of excited states in odd nuclei. Systematic errors can thus be reduced by working exclusively with binding energies.

To this end, we computed a number of one-quasi-particle (q.p.) configurations for the odd-mass neighbors of ^{16}O, ^{40}Ca, ^{48}Ca, ^{56}Ni, ^{132}Sn, and ^{208}Pb. Calculations were done at the equal filling approximation, which is an excellent approximation to the full time-reversal, symmetry-breaking blocking scheme [69]. Blocking q.p. states induces a small shape polarization [49], which in turn leads to a fragmentation of spherical s.p. orbitals of angular momentum j into $2j + 1$ levels $\Omega = -j, \ldots, +j$. In principle, the "experimental" s.p. energy should be the average energy over all the $2j + 1$ blocking configurations. However, a state with the projection Ω can belong to any spherical orbit $j \geqslant |\Omega|$, which could potentially complicate the identification for low-Ω values. We therefore associate a spherical orbit with spin j to the blocking configuration with the maximum projection $\Omega = +j$. We have verified that the amount of splitting in all these nuclei does not exceed 150 keV: For the proton $i_{13/2}$ orbit in ^{208}Pb, it is 77 keV, and for the neutron $1f_{7/2}$ state in ^{40}Ca, it is 124 keV. This implies that the error induced by cherry-picking a single state out of a $2j + 1$ nondegenerate candidate instead of the average is only on the order of 60 keV.

Figure 9 compares single-proton energies in ^{208}Pb computed with UNEDF0 and UNEDF1 with the experimental values. Although the differences between these two functionals are small, we note that UNEDF1 improves slightly the description of several high-j levels except for a too low position of the $1h_{9/2}$ proton orbit that reduces the size of the $Z = 82$ proton

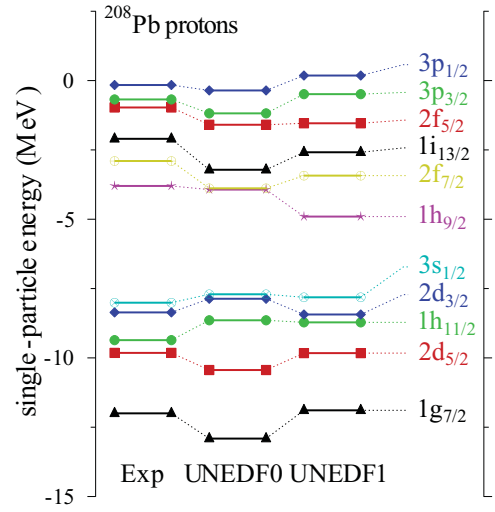

FIG. 9. (Color online) Single-proton energies for ^{208}Pb, calculated with UNEDF0 and UNEDF1 EDFs compared to the experimental values of Ref. [72].

gap. The situation is similar for the neutron single-particle energies in ^{208}Pb. For both UNEDF0 and UNEDF1 the effective mass is close to one, which probably explains the fairly good reproduction of the level density in ^{208}Pb. In the lighter doubly magic nuclei, differences between UNEDF0 and UNEDF1 s.p. energies are somewhat larger. The magic gaps in Ca isotopes are now better reproduced, although the $N = 28$ gap in ^{48}Ca is still too low.

C. Superdeformed states and fission barriers

Table IX lists the excitation energies of superdeformed (SD) fission isomers in the actinide region and SD bandheads in the mass $A \sim 190$ region calculated with the UNEDF0 and UNEDF1 parameterizations. Contrary to fission isomers, SD bandheads in neutron-deficient lead and mercury isotopes were not included in the objective function, because the prolate-oblate shape coexistence effects, not captured by current functionals, are well known in these nuclei [73,74]. Indeed, calculations with UNEDF1 predict an oblate ground state at $\beta = -0.2$ to -0.15 in all the Hg-Pb isotopes considered, coexisting with a slightly higher spherical minimum. By contrast, the ground state of the three lead isotopes is spherical with UNEDF0. The fact that the spherical configuration is disfavored in these nuclei can be traced back to a too-low $Z = 82$ spherical proton gap in UNEDF1, (Sec. V B).

All values listed in Table IX were obtained with the HFBTHO code using the same large HO basis as used for the optimization. In particular, the deformation of the basis was spherical for the ground state, and was deformed with $\beta_2 = 0.4$ for the FI; see Sec. III B. As can be seen from Table IX, the optimization improves dramatically the rms deviation for the actinide nuclei included in the fit, going from 3.02 MeV in UNEDF0 to 0.23 MeV in UNEDF1. At the same time, the optimization deteriorates the description of SD excitations in the Hg and Pb isotopes. To understand this behavior, we again compute the effective surface coefficient $a_{\rm surf}^{\rm (eff)}$ (16) for ^{194}Pb. It is particularly low, 16.0 MeV, for UNEDF1. Indeed, it is 17.64 MeV for UNEDF0, 17.1 MeV for SLy4, 16.50 MeV for BSk6, and 16.36 MeV for SkM*. In addition, the reduced $Z = 82$ magic gap in UNEDF1 energetically favors deformed and SD states. Consequently, both bulk energy and shell effects of UNEDF1 conspire to reduce the excitation energy of SD states in the Pb isotopes. In view of the major shape coexistence effects recalled earlier, this behavior is not too worrisome.

TABLE IX. Excitation energies (in MeV) of fission isomers in the actinides and superdeformed bandheads in the neutron-deficient Hg and Pb nuclei calculated with HFBTHO. The values predicted with UNEDF0 and UNEDF1 are compared with experiment.

Nucleus	UNEDF0	UNEDF1	Expt.	Ref.
^{236}U	5.28	2.42	2.75	[50]
^{238}U	5.73	2.71	2.557	[50]
^{240}Pu	5.74	2.51	2.8	[50]
^{242}Cm	5.27	1.85	1.9	[50]
^{192}Hg	6.33	2.62	5.3	[75]
^{194}Hg	7.27	3.79	6.017	[76]
^{192}Pb	5.20	1.25	4.011	[77]
^{194}Pb	5.99	1.99	4.643	[78]
^{196}Pb	7.26	3.52	5.63	[79]

In the $A \sim 190$ region, the experimental uncertainty of the SD bandhead comes from the extrapolation of the rotational band down to spin 0^+. The associated error is estimated to be very small, around 5 keV. In the actinides, experimental excitation energies of FI are usually determined with larger uncertainties. Although the experimental error bar is only about 5–10 keV for ^{236,238}U, it grows to about 200 keV for ^{240}Pu and ^{242}Cm. For the fission isomer of ^{240}Pu, recent measurements lower its excitation energy by about 500 keV to roughly 2.25 MeV [84] compared with the standard value [50] adopted in this work. Because of the relatively large uncertainty, $w_i = 0.5$ MeV, adopted for FI energies in our objective function, these experimental uncertainties are not going to significantly alter the final optimization. For future work, however, better experimental determination of FI bandheads should become a priority.

Our long-term goal is to develop an EDF that can accurately predict and describe fission observables in heavy and superheavy nuclei. We present here some results of spontaneous fission pathway calculations with UNEDF1. All fission calculations were done with version 2.49t of the code HFODD [85] that can break all self-consistent symmetries along the fission path. At each point along the collective trajectory, the HO basis deformation and frequencies are determined from a standard nuclear surface, parametrized by surface deformations $\alpha_{\lambda\mu}$. The deformations were chosen to minimize the energy as a function of the requested quadrupole moment $\overline{Q}_{20}$, according to the following expressions:

$$\begin{aligned} \alpha_{20} &= A\overline{Q}_{20}^3 + B\overline{Q}_{20}^2 + C\overline{Q}_{20}, \\ \alpha_{40} &= 0.01, \end{aligned} \tag{17}$$

with $A = 3.16721 \times 10^{-8}$ b^{-3}, $B = -2.75505 \times 10^{-5}$ b^{-2}, $C = 0.00954925$ b^{-1}, and all remaining deformations

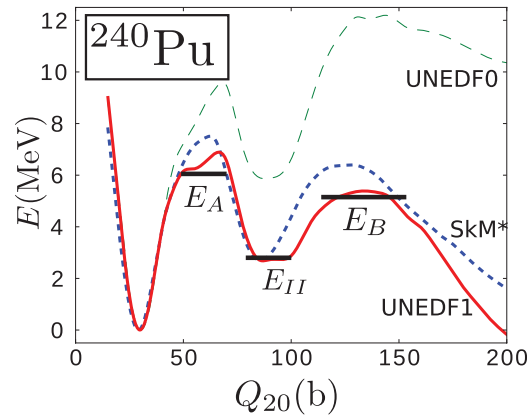

FIG. 10. (Color online) Fission pathway for ^{240}Pu along the mass quadrupole moment Q_{20} calculated using HFODD with SkM*, UNEDF0, and UNEDF1 EDFs. The ground-state energies have been normalized to zero. E_{II}, E_A, and E_B indicate, respectively, the experimental energy of fission isomer and the inner and outer barrier heights [80].

TABLE X. Empirical and theoretical inner barrier heights E_A (in MeV) for selected actinide nuclei. The rms deviations from experiment ΔE_A are shown in the last row.

Nuclide	Expt. [80]	HFB + Fit [81]	ETFSI [82]	FRLDM [83]	HFB-14 [31]	SkM*	UNEDF1
^{236}U	5.00	5.52	5.20	4.45	5.52	6.93	6.39
^{238}U	6.30	5.80	5.70	5.08	5.93	7.25	6.50
^{238}Pu	5.60	5.57	5.40	5.27	5.96	7.39	6.83
^{240}Pu	6.05	5.89	5.80	5.99	6.49	7.51	6.77
^{242}Pu	5.85	6.02	6.20	6.42	6.81	7.44	6.59
^{244}Pu	5.70	—	6.40	6.59	6.85	7.82	6.10
^{242}Cm	6.65	6.20	6.10	6.56	6.75	8.76	7.12
^{244}Cm	6.18	6.18	6.40	6.92	7.10	8.81	6.99
^{246}Cm	6.00	6.00	6.50	7.01	7.31	8.41	6.69
^{248}Cm	5.80	—	6.50	6.80	7.25	7.94	6.12
ΔE_A			0.47	0.75	0.87	1.97	0.79

$\alpha_{\lambda\mu} = 0$. The basis contains up to $N = 31$ shells and up to $N = 1140$ states. Such an extended basis was previously applied in the systematic study of fission barriers in the transfermium region and yielded excellent convergence [8,86]. We have checked that HFODD, with a reduced HO basis as compared with HFBTHO calculations, reproduces the HFBTHO energies of FI bandheads in Table IX with an accuracy of 100–200 keV. We consider this agreement satisfactory considering other uncertainties involved.

As an example, Fig. 10 displays the potential energy curve of ^{240}Pu as a function of the mass quadrupole moment Q_{20}. Triaxiality and reflection asymmetry effects are included for all calculations. The large-deformation behavior of the potential energy curve obtained by UNEDF0 is typical in this region, so that the outer barrier heights obtained by UNEDF0 are systematically much higher than empirical values. We note that the UNEDF1 functional yields both the inner and outer barrier in ^{240}Pu fairly close to experiment. Both UNEDF0 and UNEDF1 functionals also yield the g.s. binding energy that is close to the empirical value.

The UNEDF1 results for fission barrier heights in selected actinide nuclei are listed in Tables X (inner barrier) and XI (outer barrier). For comparison, we also list the empirical barrier heights from the Reference Input Parameter Library (RIPL-3) [80]; the HFB fission barriers obtained by fitting the neutron-induced fission cross section [81]; and predictions of ETFSI [82], FRLDM [83], and HFB-14 [31] models, together with HFODD calculations with the SkM* EDF. (For SkM* predictions including the energy correction from the rotational zero-point motion; see Ref. [6].) Overall, the description of experimental data by UNEDF1 is very reasonable, with the rms deviations from experimental values of E_A and E_B comparable to the values obtained in more phenomenological models. One can thus conclude that fission barriers are reliably described at the HFB level with the UNEDF1 functional. This result is remarkable because it was obtained by adding only four excitation energies to the data set.

There seems to exist an interesting relation between barrier heights and the surface thickness. We have evaluated the surface thickness in ^{208}Pb from the charge form factor $\sigma_{\rm ch}$ as defined, for example, in Refs. [4,23] and found $\sigma_{\rm ch} = 0.932$ fm for UNEDF0 and $\sigma_{\rm ch} = 0.907$ fm for UNEDF1. This is to be compared with the measured value of $\sigma_{\rm ch} = 0.913$ fm [23]. It is apparent that the EDF which does well on fission barriers also performs well for surface thickness. The functionals SV-min and SV-bas which included $\sigma_{\rm ch}$ in the fit, and yield values around 0.91 fm for this quantity, happen to perform well concerning barrier heights [48]. The relation between fission barriers and surface thickness deserves closer inspection in future work.

TABLE XI. Similar to Table X except for the outer barrier heights E_B (in MeV).

Nuclide	Expt. [80]	HFB + Fit [81]	ETFSI [82]	FRLDM [83]	HFB-14 [31]	SkM*	UNEDF1
^{236}U	5.67	6.03	4.00	5.03	6.03	6.70	5.56
^{238}U	5.50	6.17	4.90	5.64	6.48	7.36	6.42
^{238}Pu	5.10	5.35	2.90	4.47	5.24	5.99	4.62
^{240}Pu	5.15	5.73	3.40	4.91	5.61	6.40	5.42
^{242}Pu	5.05	5.61	3.60	5.72	6.02	6.90	6.20
^{244}Pu	4.85	—	3.90	6.47	6.25	7.49	6.50
^{242}Cm	5.00	4.90	1.70	4.45	4.51	6.31	4.08
^{244}Cm	5.10	5.10	2.10	5.07	4.83	7.00	5.03
^{246}Cm	4.80	4.80	2.40	5.87	5.23	7.42	5.51
^{248}Cm	4.80	—	2.60	6.65	5.25	7.32	5.55
ΔE_B			2.11	0.94	0.70	1.89	0.84

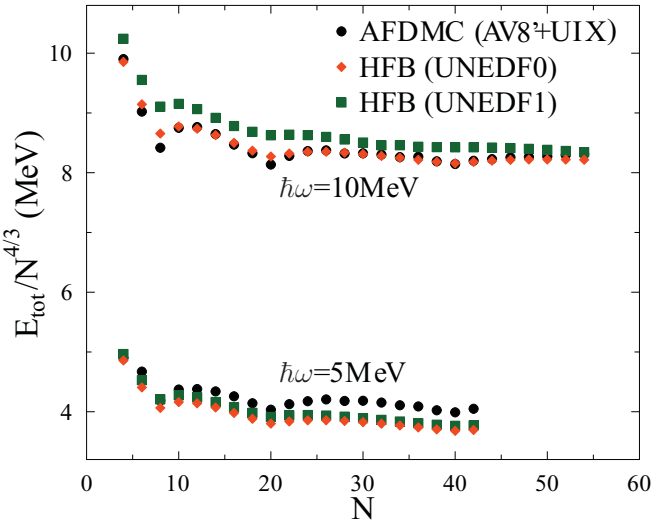

FIG. 11. (Color online) Comparison of UNEDF0 and UNEDF1 predictions for the energy N-neutron drops trapped in an HO potential with $\hbar\omega = 5$ MeV and 10 MeV with the AFDMC *ab initio* results of Ref. [88].

D. Neutron drops

Recently, there has been a considerable interest in studies of inhomogeneous neutron matter by considering finite systems of N neutrons, specifically, neutron drops [87,88]. Because neutron drops are not self-bound [89], an external potential must be used to confine them. By studying neutron drops, one can test different *ab initio* approaches and their correspondence to DFT calculations [87,88]; investigate the validity of the density matrix expansion [90]; and develop a theoretical link between neutron-rich nuclei and the neutron matter found in the neutron star crust [91].

Figure 11 presents the results of UNEDF0 and UNEDF1 calculations for neutron drops confined by two external HO traps with $\hbar\omega = 5$ MeV and 10 MeV. The DFT results are compared with *ab initio* AFDMC benchmark calculations of Ref. [88] employing the AV8′ nucleon-nucleon and Urbana IX three-nucleon force. As can be seen, UNEDF0 reproduces AFDMC results well, especially because the functional was not constrained to finite neutron matter. The agreement with UNEDF1 calculations is also good, especially for a softer trap with $\hbar\omega = 5$ MeV.

In future EDF optimizations we shall include *ab initio* predictions for neutron drops into the data set. By providing unique constraints on finite neutron matter, such pseudodata are expected to improve the description of very neutron-rich nuclei and diluted neutron matter. The results shown in Fig. 11 indicate that UNEDF0 and UNEDF1 functionals represent excellent starting points for such optimizations.

VI. CONCLUSIONS

By performing nuclear energy density optimization at the deformed HFB level, we have arrived at the new Skyrme parameterization UNEDF1. Our main focus was to improve the description of fission properties of the actinide nuclei and to provide a high-quality functional for time-dependent applications involving heavy systems. The only notable change in the form of the energy density as compared with our previous work [25] was the removal of the center-of-mass correction. For the χ^2 minimization, we used the derivative-free POUNDerS algorithm. Compared with UNEDF0, the data set was enlarged by adding ground-state masses of three deformed actinide nuclei and excitation energies of fission isomers in ^{236,238}U, ^{240}Pu, and ^{242}Cm. For the optimal parameter set, we carried out a sensitivity analysis to obtain information about the standard deviations and correlations among the parameters. We conclude that UNEDF1 remains as robust under a change of individual data as UNEDF0.

Overall, UNEDF1 provides a description of global nuclear properties that is almost as good as that of UNEDF0. Not surprising, the quality of data reproduction is slightly degraded: By adding a new type of data (fission isomers), one is likely to worsen the fit for other observables. The most striking feature of UNEDF1 is its ability to reproduce the empirical fission barriers in the actinide region. We find it encouraging that, by including only a handful of fission isomer bandheads, deformation properties of the functional seem well constrained. Another unanticipated property of UNEDF0 and UNEDF1 is their ability to reproduce *ab initio* results for trapped neutron drops. This is significant because such pseudodata will be used in future EDF optimizations.

In addition to imposing new constraints on neutron drops, in the next step we intend to improve the spectroscopic quality of UNEDF functionals by considering the experimental data on spin-orbit splittings and shell gaps. We shall also improve the density dependence of the kinetic term by adding new constraints on giant resonances. Meanwhile, the functional UNEDF1 developed in this work will be the input of choice for microscopic studies of the nuclear fission process.

ACKNOWLEDGMENTS

We are grateful to A. Staszczak and J. Moré for helpful discussions. This work was supported by the US Department of Energy under Contracts No. DE-FC02-09ER41583 (UNEDF SciDAC Collaboration), No. DE-FG02-96ER40963 (University of Tennessee), No. DE-FG52-09NA29461 (the Stewardship Science Academic Alliances program), No. DE-AC07-05ID14517 (NEUP subaward Grant No. 00091100), and No. DE-AC0Z-06CA11357 (Argonne National Laboratory), and was partly performed under the auspices of the US Department of Energy by Lawrence Livermore National Laboratory under Contract No. DE-AC52-07NA27344. Funding was also provided by the US Department of Energy Office of Science, Nuclear Physics Program pursuant to Contract No. DE-AC52-07NA27344 Clause B-9999, Clause H-9999, and the American Recovery and Reinvestment Act, Pub. L. 111-5. Computational resources were provided through an INCITE award "Computational Nuclear Structure" by the National Center for Computational Sciences (NCCS) and National Institute for Computational Sciences (NICS) at Oak Ridge National Laboratory, and through an award by the Laboratory Computing Resource Center at Argonne National Laboratory.

[1] G. F. Bertsch, D. J. Dean, and W. Nazarewicz, SciDAC Review **6**, 42 (2007).
[2] R. Furnstahl, Nucl. Phys. News. **21**, 2 (2011).
[3] P. Möller, D. G. Madland, A. J. Sierk, and A. Iwamoto, Nature (London) **409**, 785 (2001).
[4] M. Bender, P.-H. Heenen, and P.-G. Reinhard, Rev. Mod. Phys. **75**, 121 (2003).
[5] T. Bürvenich, M. Bender, J. A. Maruhn, and P.-G. Reinhard, Phys. Rev. C **69**, 014307 (2004).
[6] L. Bonneau, P. Quentin, and D. Samsoen, Eur. Phys. J. A **21**, 391 (2004).
[7] M. Samyn, S. Goriely, and J. M. Pearson, Phys. Rev. C **72**, 044316 (2005).
[8] A. Staszczak, A. Baran, J. Dobaczewski, and W. Nazarewicz, Phys. Rev. C **80**, 014309 (2009).
[9] J. A. Sheikh, W. Nazarewicz, and J. C. Pei, Phys. Rev. C **80**, 011302(R) (2009).
[10] N. Schindzielorz, J. Erler, P. Klüpfel, P.-G. Reinhard, and G. Hager, Int. J. Mod. Phys. E **18**, 773 (2009).
[11] M. Warda, J. L. Egido, L. M. Robledo, and K. Pomorski, Phys. Rev. C **66**, 014310 (2002).
[12] H. Goutte, J. F. Berger, P. Casoli, and D. Gogny, Phys. Rev. C **71**, 024316 (2005).
[13] N. Dubray, H. Goutte, and J.-P. Delaroche, Phys. Rev. C **77**, 014310 (2008).
[14] W. Younes and D. Gogny, Phys. Rev. C **80**, 054313 (2009).
[15] K. Rutz, J. A. Maruhn, P.-G. Reinhard, and W. Greiner, Nucl. Phys. A **590**, 680 (1995).
[16] H. Abusara, A. V. Afanasjev, and P. Ring, Phys. Rev. C **82**, 044303 (2010).
[17] J. Dobaczewski, J. Phys. G **36**, 105105 (2009).
[18] G. Hupin, D. Lacroix, and M. Bender, Phys. Rev. C **84**, 014309 (2011).
[19] G. F. Bertsch, B. Sabbey, and M. Uusnäkki, Phys. Rev. C **71**, 054311 (2005).
[20] T. Nikšić, D. Vretenar, and P. Ring, Phys. Rev. C **78**, 034318 (2008).
[21] M. Kortelainen, J. Dobaczewski, K. Mizuyama, and J. Toivanen, Phys. Rev. C **77**, 064307 (2008).
[22] S. Goriely, N. Chamel, and J. M. Pearson, Phys. Rev. Lett. **102**, 152503 (2009).
[23] P. Klüpfel, P.-G. Reinhard, T. J. Burvenich, and J. A. Maruhn, Phys. Rev. C **79**, 034310 (2009).
[24] P.-G. Reinhard and W. Nazarewicz, Phys. Rev. C **81**, 051303(R) (2010).
[25] M. Kortelainen, T. Lesinski, J. Moré, W. Nazarewicz, J. Sarich, N. Schunck, M. V. Stoitsov, and S. Wild, Phys. Rev. C **82**, 024313 (2010).
[26] N. Nikolov, N. Schunck, W. Nazarewicz, M. Bender, and J. Pei, Phys. Rev. C **83**, 034305 (2011).
[27] F. Tondeur, M. Brack, M. Farine, and J. M. Pearson, Nucl. Phys. A **420**, 297 (1984).
[28] C. Guet, H.-B. Håkansson, and M. Brack, Phys. Lett. B **97**, 7 (1980).
[29] J. Bartel, P. Quentin, M. Brack, C. Guet, and H.-B. Håkansson, Nucl. Phys. A **386**, 79 (1982).
[30] J.-F. Berger, M. Girod, and D. Gogny, Nucl. Phys. A **502**, 85c (1989).
[31] S. Goriely, M. Samyn, and J. M. Pearson, Phys. Rev. C **75**, 064312 (2007).
[32] E. Perlińska, S. G. Rohoziński, J. Dobaczewski, and W. Nazarewicz, Phys. Rev. C **69**, 014316 (2004).
[33] S. G. Rohoziński, J. Dobaczewski, and W. Nazarewicz, Phys. Rev. C **81**, 014313 (2010).
[34] J. Dobaczewski, W. Nazarewicz, and M. V. Stoitsov, Eur. Phys. J. A **15**, 21 (2002).
[35] G. F. Bertsch, C. A. Bertulani, W. Nazarewicz, N. Schunck, and M. V. Stoitsov, Phys. Rev. C **79**, 034306 (2009).
[36] J. Dobaczewski, H. Flocard, and J. Treiner, Nucl. Phys. A **422**, 103 (1984).
[37] M. V. Stoitsov, J. Dobaczewski, W. Nazarewicz, S. Pittel, and D. J. Dean, Phys. Rev. C **68**, 054312 (2003).
[38] A. Bohr and B. R. Mottelson, *Nuclear Structure*, Vol. II (Benjamin, New York, 1975).
[39] P. Ring and P. Schuck, *The Nuclear Many Body Problem* (Springer-Verlag, New York, 1980).
[40] M. Bender, K. Rutz, P.-G. Reinhard, and J. A. Maruhn, Eur. Phys. J. A **7**, 467 (2000).
[41] J.-F. Berger and D. Gogny, Nucl. Phys. A **333**, 283 (1980).
[42] J. Skalski, Phys. Rev. C **76**, 044603 (2007).
[43] J. Skalski, Int. J. Mod. Phys. E **17**, 151 (2008).
[44] W. Younes and D. Gogny, Phys. Rev. Lett. **107**, 132501 (2011).
[45] A. S. Umar and V. E. Oberacker, Phys. Rev. C **73**, 054607 (2006).
[46] A. S. Umar and V. E. Oberacker, J. Phys. G **36**, 025101 (2009).
[47] K.-H. Kim, T. Otsuka, and P. Bonche, J. Phys. G **23**, 1267 (1997).
[48] J. Erler, P. Klüpfel, and P.-G. Reinhard, J. Phys. G: Nucl. Part. Phys. **37**, 064001 (2010).
[49] M. Zalewski, J. Dobaczewski, W. Satuła, and T. R. Werner, Phys. Rev. C **77**, 024316 (2008).
[50] B. Singh, R. Zywina, and R. B. Firestone, Nucl. Data Sheets **97**, 241 (2002).
[51] E. Chabanat, P. Bonche, P. Haensel, J. Meyer, and R. Schaeffer, Nucl. Phys. A **635**, 231 (1998).
[52] M. V. Stoitsov, J. Dobaczewski, W. Nazarewicz, and P. Ring, Comput. Phys. Commun. **167**, 43 (2005).
[53] J. A. Nelder and R. Mead, Computer J. **7**, 308 (1965).
[54] T. Lesinski, K. Bennaceur, T. Duguet, and J. Meyer, Phys. Rev. C **74**, 044315 (2006).
[55] M. Kortelainen and T. Lesinski, J. Phys. G: Nucl. Part. Phys. **37**, 064039 (2010).
[56] J. Moré and S. M. Wild, ACM Trans. Math. Soft. **38** (to be published).
[57] S. Goriely and J. M. Pearson, Phys. Rev. C **77**, 031301 (2008).
[58] B. A. Brown, Phys. Rev. C **58**, 220 (1998).
[59] S. A. Fayans, JETP Lett. **68**, 169 (1998).
[60] A. Bulgac and V. R. Shaginyan, Nucl. Phys. A **601**, 103 (1996).
[61] A. Bulgac and V. R. Shaginyan, Phys. Lett. B **469**, 1 (1999).
[62] J. Le Bloas, M.-H. Koh, P. Quentin, L. Bonneau, and J. I. A. Ithnin, Phys. Rev. C **84**, 014310 (2011).
[63] M. Kortelainen, R. J. Furnstahl, W. Nazarewicz, and M. V. Stoitsov, Phys. Rev. C **82**, 011304 (2010).
[64] P.-G. Reinhard, M. Bender, W. Nazarewicz, and T. Vertse, Phys. Rev. C **73**, 014309 (2006).
[65] S. Goriely, M. Samyn, and M. Bender, and J. M. Pearson, Phys. Rev. C **68**, 054325 (2003).
[66] K. Pomorski and J. Dudek, Phys. Rev. C **67**, 044316 (2003).
[67] M. Anguiano, J. L. Egido, and L. M. Robledo, Nucl. Phys. A **683**, 227 (2001).
[68] T. Lesinski, T. Duguet, K. Bennaceur, and J. Meyer, Eur. Phys. J. A **40**, 121 (2009).

[69] N. Schunck, J. Dobaczewski, J. McDonnell, J. Moré, W. Nazarewicz, J. Sarich, and M. V. Stoitsov, Phys. Rev. C **81**, 024316 (2010).
[70] G. Colò, H. Sagawa, and P. F. Bortignon, Phys. Rev. C **82**, 064307 (2010).
[71] E. Litvinova, P. Ring, and V. Tselyaev, Phys. Rev. C **75**, 064308 (2007).
[72] N. Schwierz, I. Wiedenhover, and A. Volya, arXiv:0709.3525 (to be published).
[73] J. L. Wood, K. Heyde, W. Nazarewicz, M. Huyse, and P. van Duppen, Phys. Rep. **215**, 101 (1992).
[74] W. Nazarewicz, Phys. Lett. B **305**, 195 (1993).
[75] A. Lopez-Martens, F. Hannachi, T. Dossing, C. Schück, R. Collatz, E. Gueorguieva, Ch. Vieu, S. Leoni, B. Herskind, T. L. Khoo, T. Lauritsen, I. Ahmad, D. J. Blumenthal, M. P. Carpenter, D. Gassmann, R. V. F. Janssens, D. Nisius, A. Korichi, C. Bourgeois, A. Astier, L. Ducroux, Y. Le Coz, M. Meyer, N. Redon, J. F. Sharpey-Schafer, A. N. Wilson, W. Korten, A. Bracco, and R. Lucas, Phys. Rev. Lett. **77**, 1707 (1996).
[76] R. G. Henry, T. Lauritsen, T. L. Khoo, I. Ahmad, M. P. Carpenter, B. Crowell, T. Døssing, R. V. F. Janssens, F. Hannachi, A. Korichi, C. Schuck, F. Azaiez, C. W. Beausang, R. Beraud, C. Bourgeois, R. M. Clark, I. Deloncle, J. Duprat, B. Gall, H. Hubel, M. J. Joyce, M. Kaci, Y. Lecoz, M. Meyer, E. S. Paul, N. Perrin, N. Poffe, M. G. Porquet, N. Redon, H. Sergolle, J. F. Sharpey-Schafer, J. Simpson, A. G. Smith, R. Wadsworth, and P. Willsau, Phys. Rev. Lett. **73**, 777 (1994).
[77] E. A. Henry, A. Kuhnert, J. A. Becker, M. J. Brinkman, T. F. Wang, J. A. Cizewski, W. Korten, F. Azaiez, M. A. Deleplanque, R. M. Diamond, J. E. Draper, W. H. Kelly, A. O. Macchiavelli, and F. S. Stephens, Z. Phys. A **338**, 469 (1991).
[78] K. Hauschild, L. A. Bernstein, J. A. Becker, D. E. Archer, and R. W. Bauer, D. P. McNabb, J. A. Cizewski, K.-Y. Ding, W. Younes, R. Krücken, R. M. Diamond, R. M. Clark, P. Fallon, I.-Y. Lee, A. O. Macchiavelli, R. MacLeod, G. J. Schmid, M. A. Deleplanque, F. S. Stephens, and W. H. Kelly, Phys. Rev. C **55**, 2819 (1997).
[79] A. N. Wilson, A. K. Singh, H. Hübel, P. M. Davidson, A. Görgen, D. Roßbach, A. Korichi, A. Astier, F. Azaiez, D. Bazzacco, C. Bourgeois, N. Buforn, A. P. Byrne, G. D. Dracoulis, F. Hannachi, K. Hauschild, W. Korten, T. Kröll, G. J. Lane, A. Lopez-Martens, N. Redon, P. Reiter, C. Rossi-Alvarez, G. Schonwaßer, O. Stezowski, and P. G. Thirolf, Phys. Rev. Lett. **95**, 182501 (2005).
[80] R. Capote, M. Herman, P. Obložinský, P. G. Young, S. Goriely, T. Belgya, A. V. Ignatyuk, A. J. Koning, S. Hilaire, V. A. Plujko, M. Avrigeanu, O. Bersillon, M. B. Chadwick, T. Fukahori, Zhigang Ge, Yinlu Han, S. Kailas, J. Kopecky, V. M. Maslov, G. Reffo, M. Sin, E. Sh. Soukhovitskii, and P. Talou, Nucl. Data Sheets **110**, 3107 (2009); Reference Input Parameter Library (RIPL-3) [http://www-nds.iaea.org/RIPL-3/].
[81] S. Goriely, S. Hilaire, A. J. Koning, M. Sin, and R. Capote, Phys. Rev. C **79**, 024612 (2009).
[82] A. Mamdouh, J. M. Pearson, M. Rayet, and F. Tondeur, Nucl. Phys. A **679**, 337 (2001).
[83] P. Möller, A. J. Sierk, T. Ichikawa, A. Iwamoto, R. Bengtsson, H. Uhrenholt, and S. Åberg, Phys. Rev. C **79**, 064304 (2009).
[84] M. Hunyadi, D. Gassmann, A. Krasznahorkay, D. Habs, P. G. Thirolf, M. Csatlós, Y. Eisermann, T. Faestermann, G. Graw, J. Gulyás, R. Hertenberger, H. J. Maier, Z. Máté, A. Metz, and M. J. Chromik, Phys. Lett. B **505**, 27 (2001).
[85] N. Schunck, J. Dobaczewski, J. McDonnell, W. Satuła, J. A. Sheikh, A. Staszczak, M. Stoitsov, and P. Toivanen, Comp. Phys. Comm. **183**, 166 (2012).
[86] A. Staszczak, J. Dobaczewski, and W. Nazarewicz, Int. J. Mod. Phys. E **14**, 395 (2005).
[87] B. S. Pudliner, A. Smerzi, J. Carlson, V. R. Pandharipande, S. C. Pieper, and D. G. Ravenhall, Phys. Rev. Lett. **76**, 2416 (1996).
[88] S. Gandolfi, J. Carlson, and S. C. Pieper, Phys. Rev. Lett. **106**, 012501 (2011).
[89] S. C. Pieper, Phys. Rev. Lett. **90**, 252501 (2003).
[90] S. K. Bogner, R. J. Furnstahl, H. Hergert, M. Kortelainen, P. Maris, M. Stoitsov, and J. P. Vary, Phys. Rev. C **84**, 044306 (2011).
[91] D. G. Ravenhall, C. J. Pethick, and J. R. Wilson, Phys. Rev. Lett. **50**, 2066 (1983).